Effect of cold rolling on phase separation in 2202 lean duplex stainless steel

S. Cazottes, V. Massardier, Raphaële Danoix, D. Rolland, S. Cissé, Frederic Danoix

Effect of cold rolling on phase separation in 2202 lean duplex stainless steel

S. Cazottes[a,*], V. Massardier[a], R. Danoix[c], D. Rolland[a], S. Cissé[b], F. Danoix[c]

[a] Univ Lyon, CNRS, INSA-Lyon, MATEIS UMR5510, F-69621 Villeurbanne, France
[b] INDUSTEEL, 56 rue Clémenceau Le Creusot, 72100, France
[c] Normandie University, UNIROUEN, INSA Rouen, CNRS, Groupe de Physique des Matériaux, F-76000 Rouen, France

ARTICLE INFO

Keywords:
Lean duplex stainless steels
Ferrite decomposition
Cold rolling
Atom probe tomography
Thermoelectric power

ABSTRACT

The effect of plastic deformation (cold rolling) on the thermal aging of a lean 2202 duplex stainless steel at intermediate temperatures (280 °C–450 °C) was studied using a combination of atom probe tomography and thermoelectric power measurements. In the undeformed condition, spinodal decomposition of ferrite was shown to be the prime aging process with an activation energy of 206 kJ/mol. Plastic deformation enhanced the aging and the austenite partly transformed into martensite. When no precipitation or phase transformation was observed in austenite, both ferrite and martensite decomposed. The spinodal decomposition kinetics of ferrite increased with increasing deformation rate. The FeCr-rich martensite also decomposed at 450 °C, via a nucleation and growth process, owing to a decrease of the Cr content in the matrix. Chromium nitrides, G-Phase, and Cu-rich precipitates were observed in the decomposed martensite.

1. Introduction

Lean duplex stainless steels (DSSs) were developed in the late 1990s to have a cheaper option of materials with similar mechanical corrosion properties to counterpart standard austenitic stainless steels (such as AISI 304 or 316) [1,2]. So, lean grades can often replace common 30x grades of the austenitic stainless steel family while the higher-alloyed standard grade of duplex stainless steel, namely 2205, was designed to replace grade 316 austenitic stainless steel. They contain lower Ni, Mo, and Cr contents than the 2205 standard DSS but higher Mn and N contents to maintain a ferrite/austenite ratio close to one.

The ferritic phase in lean DSSs contains approximately 24 at% Cr [3] and undergoes ferrite decomposition for aging temperatures between room temperature (RT) and 500 °C [4]. This well-documented phenomenon [5–10] is responsible for the embrittlement observed in aged Fe–Cr and stainless steels that contain ferrite and martensite in this temperature range . The initially homogeneous ferrite[1] decomposes into iron-rich alpha (α) and chromium-rich alpha prime (α') domains at the nanometric scale. Two mechanisms for this phase separation are possible: a continuous mechanism (spinodal decomposition) or a discrete mechanism (nucleation and growth, of α' precipitates) [11]. To discriminate between these mechanisms, the time evolution of the Cr content wavelength and amplitude must be tracked as a function of time in the early stages, with spinodal decomposition showing $t^{0.15–0.20}$ behavior and nucleation and growth showing $t^{0.33}$ behavior. However, from a microstructural viewpoint, for most Cr contents, the spinodal decomposition leads to an interconnected (or sponge-like) structure, forming a continuous network of α' zones whose Cr content increases with aging time until reaching the equilibrium composition predicted by the phase diagram. The nucleation and growth mechanism occurs through the development of isolated particles of the same α' phase, which is theoretically predicted to reach the equilibrium composition from the beginning. These morphological differences are commonly used to discriminate between the SD and NG mechanisms. However, even for low Cr content, de-percolation of the α' network can occur, and the morphology of the spinodally decomposed domains can be visually very similar to that formed by the NG mechanism. For 2205 and 2003 DSSs, a spinodal mechanism was reported for temperatures ranging from 250 °C to 450 °C [4,12,13].

The decomposition rate in Fe–Cr alloys is well documented [5–7,9,10] and is affected by both the aging temperature and alloy composition. Applied elastic stress is also known to affect the decomposition mechanism [14]. Phase-field simulation has shown that the morphology of the decomposed phases is dependent on the load direction relative to the crystal direction [15]. Indeed, under applied stress, the α' domains tend to align along elastic soft directions; therefore, the morphology of the decomposed structure is greatly affected by the amount of stress and the strain orientation. Recent atom probe tomography (APT) experiments revealed an increase in the kinetics of phase separation with applied load in a 15–5 PH martensitic stainless steel aged at 450 °C

* Corresponding author.
E-mail address: sophie.cazottes@insa-lyon.fr (S. Cazottes).

[1] In DSSs, the ferrite is called either delta or alpha ferrite. In this paper we use alpha as we are interested in intermediate temperature ageing, for which alpha is the commonly used terminology.

https://doi.org/10.1016/j.mtla.2020.100854
Received 29 May 2020; Accepted 27 July 2020

Table 1
Chemical composition of the studied duplex stainless steel.

	Fe	C	Cr	Ni	Mn	Mo	N
wt%	Bal.	<0.03	22–23.8	2–2.8	<2	<0.45	0.16–0.26
at%	Bal.	<0.11	23–25	1.8–2.6	<2	<0.26	0.63–1.01

[16]. In that case, the phase separation occurred via a NG mechanism. Moreover, the decomposition kinetics appeared to be affected by the orientation of the load relative to the crystal orientation; however, no clear orientation or elongation of the Cr-rich precipitates was observed. Zhou et al. also reported an effect of strain on the phase separation kinetics in DSS welds [17].

The phase separation observed in the Fe–Cr system leads to a significant loss of ductility and increase in hardness and yield strength, resulting in embrittlement of the steel [18–21]. It is thus essential to characterize the decomposition kinetics of the ferrite to predict the evolution of the material properties under service conditions. The phase separation in DSSs has been shown to be faster than that in Fe–Cr binary systems of the same Cr content [6] and therefore requires systematic characterization [9]. In particular, the effect of the deformation on the decomposition kinetics is not yet well documented for DSSs steels. Moreover, it is well known that in DSS steels, austenite transforms into martensite upon deformation [22]. This martensite contains around 15 wt% of Cr and is also prone to phase separation.

The aim of this paper is to study the effect of plastic deformation on the phase separation kinetics of ferrite in lean DSSs at intermediate temperature. First, the phase separation kinetics of a 2202 commercial alloy was followed using a global technique; thermoelectric power (TEP) measurements. Indeed, this global measurement technique is very sensitive to microstructural evolution in metallic material [23–25] and can be used to determine the activation energies responsible for demixion [4,26]. As this method requires data from three different temperatures, and in order to cover the temperature range for which phase separation was observed, the samples were aged at 280 °C, 350 °C and 480 °C. The phase separation products were then characterized using APT.

Secondly, the same alloy was then cold rolled to different deformation levels (0, 30% and 50%) and subsequently aged at 450 °C. Large differences in deformation levels and a high temperature were chosen in order to maximize the phase separation phenomenon for a limited ageing time. The kinetics of phase separation was also followed by TEP, and the decomposition products were characterized by APT. The effects of plastic deformation on the α–α' phase separation is discussed.

2. Material and methods

2.1. Material and thermal treatments

The as-received material was a 12-mm-thick hot-rolled sheet of UR2202 (S32202 × 2XrNiN22-2) lean DSS. The composition of the steel is shown in Table 1. The ferrite to austenite ratio of this commercial alloy in the as-received state was close to 1.

2.2. Experimental procedure

To study the effect of plastic deformation on ferrite phase separation kinetics, the as-received material was cold rolled along the prior transverse direction (TD) of the plate, as illustrated in Fig. 1, to achieve thickness reductions of 30% and 50%. The microstructure after deformation was characterized by electron backscatter diffraction (EBSD) performed using a Zeiss Supra 55VP FEG SEM operated at 15 kV and equipped with an Oxford Instrument Symmetry EBSD camera using a step size of 0.5 μm. Map sizes are around 300 × 200 μm^2. The post processing and data treatment was performed using Channel5 software and ATEX software [27]. A standard post processing was performed, with the removal of all isolated pixels, and a correction up to four similar neighbors. The samples were prepared by classical mechanical polishing (down to a 1-μm diamond paste), followed by 20-min vibratory polishing using a Buehler Mastermet2 colloidal suspension.

The aging kinetics of the studied steel was followed using TEP measurements after aging at 280 °C, 350 °C, 450 °C, and 500 °C from 1 min up to 1086 h in salt baths. The apparatus provides the TEP of the steel relative to that of pure iron. The principle of the technique is described in [28]. For each investigated temperature T, the TEP, denoted S, of a sample of dimensions 60 × 3 × 1 mm^3 was measured before any heat treatment ($S(T,t_0)$) and after different aging times t ($S(T,t)$). The variation of TEP with time $\Delta S(T,t) = S(T,t) - S(T,t_0)$ was then plotted for the different aging temperatures. In the present case, the TEP variation can be attributed to the alloying elements leaving the solid solution or to the formation of precipitates (if they are small and coherent). All the measurements were repeated for each time step.

The nature of the aging products was characterized using APT. Parallepipedic samples with dimensions of 0.3 × 0.3 × 20 mm^3 were cut after grinding both initial 'TD' faces. The samples were subsequently thinned using the standard two-stage electrolytic polishing process to obtain sharp tips suitable for APT analysis [29]. The analyses were performed using a LEAP® 4000HR in voltage mode at 50 K with a pulse-to-standing-voltage ratio of 20%, a nominal pulse repetition rate of 200 kHz, and a detection rate of 0.5%. The data were analyzed using IVAS 3.8 software. The reconstruction parameters used in this study included an image compression factor (m+1) of 1.6 and a k factor of 4.1. Measurement of the compositions of the different phases relies on the identification of the mass peaks of mass spectra. As several overlaps occur in the mass spectra of this complex alloy and may depend on the analyzed phase, identification of the various peaks will be discussed in detail (Section 3.4.1). Ferrite and austenite were primary identified in aged samples from the presence or absence of fluctuations of the Cr content. Their identification was then confirmed by their respective Ni, N, Mo, and Mn contents. As will be shown later (Section 3.4.3), the obtained microstructure of the aged ferrite consisted of interconnected α' networks. Two independent parameters were used to characterize the progress of the α–α' decomposition in ferrite: frequency distribution analysis of the Cr content fluctuations and the associated variation parameter (V) [4,7,16,29] and the characteristic wavelength of the microstructure formed, calculated using autocorrelation of presented concentration profiles [30]. The parameter V is introduced to investigate the phase separation at the nanometer scale. This metric measures the absolute area difference between the experimental frequency distribution of observed given Cr contents and the corresponding binomial distribution, representing the random distribution of this element. The V parameter increases from 0 for a purely random solid solution up to 2 for extreme phase-separation cases. It should be noted that because of statistical fluctuations, experimental and binomial distributions are never identical but are considered similar when V remains smaller than 0.02–0.03.

3. Results

3.1. Microstructures before aging: effect of cold rolling

In the as-received state, the banded structure typically observed in DSS sheets was present. Using a log normal fitting based on the surface of the grains, the equivalent ferrite grain diameter was measured to be 45μm, while the austenite mean diameter 12 μm. Note that due to the small size of the maps, the ferrite grain diameter is underestimated as the larger grains are cut. After deformation, the bands elongated in the rolling direction; thinner and longer bands were therefore clearly visible. During deformation, the austenite partly transformed into martensite [22,31,32]. As martensite usually consists of micrometric lathes and as the defect density is high in this phase, a small step size and larger acquisition times were required for satisfactory indexing of this phase.

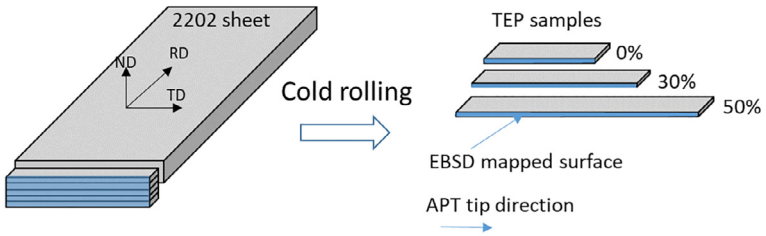

Fig. 1. Rolling procedure. The sheet was rolled along the initial TD direction to obtain the TEP sample. The EBSD mapped surface is shown in blue, and the APT tip direction is the initial TD direction. (ND: Initial Normal Direction, TD: initial Transverse Direction, and RD: initial Rolling direction).

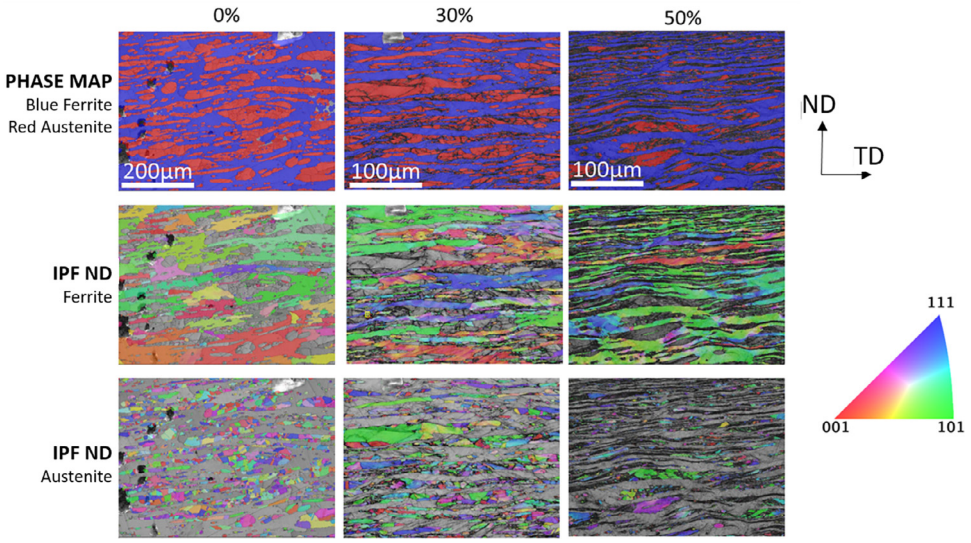

Fig. 2. EBSD characterization of the effect of cold rolling on the microstructure. 0% corresponds to the as received state, (ND and TD stands for initial normal and transverse directions respectively). 30% deformation and 50% deformation are the samples after 30% and 50% thickness reduction by cold rolling along the initial TD. (a) Phase maps, Blue = ferrite, Red=Austenite, (b) Inverse Pole Figure together with Band Contrast maps of the ferrite phase, (c) Inverse Pole Figure together with Band Contrast maps of the austenitic phase.

In the current case, a rather large step size was selected to map areas large enough to visualize several grains; as a result, the martensite was hardly indexed (Fig. 2).

However, a rough estimate of the different phase contents was made by assuming that all the non-indexed zones correspond to the martensitic phase. This very basic assumption cannot provide accurate values but allowed for a rough estimate of the volume fraction of the different phases, which could be used to interpret the TEP signal evolution presented later. An experimental ratio of 57/43 ferrite/austenite was determined. The martensite content in the 30% and 50% deformed samples was approximately 5% and 30%, respectively. These values are consistent with those observed in a LDX 2101 steel by Bassani et al., where the martensite transformation started just after 20% thickness reduction and 20% martensite was observed for 50% thickness reduction [31].

3.2. Evolution of TEP during aging

The evolution of the TEP (ΔS) as a function of time for the undeformed sample, measured during isothermal aging between 280 °C and 500 °C, is presented in Fig. 3a. For all temperatures, the TEP increased with time. This behavior was previously observed by Coste et al. [33] and Massoud et al. [34] for low-temperature aging of as-cast Fe–Cr–Ni DSS and was attributed to the spinodal decomposition of the ferritic phase and the precipitation of intermetallic G-phase particles rich in Si and Ni [33]. At 280 °C, the change of the TEP after 1000 h of aging was only 0.12 µV/°C, which is extremely small. This result was expected as the phase separation in Fe–Cr alloys is very slow at 300 °C, and no other microstructural change is expected in this temperature range. At higher temperatures, a similar evolution was observed at 350 °C and 400 °C, with TEP increases of 0.58 and 1.4 µV/°C, respectively, after 1086 h of aging. However, an important acceleration of the phase separation process between these temperatures was observed, as the same TEP value was obtained after 1086 h of aging at 350 °C and 8 h of aging at 450 °C.

The acceleration of the TEP kinetics with aging temperature suggests that the microstructural changes responsible for the TEP change are diffusion-driven processes and thus thermally activated. The activation energy can be determined by performing a time–temperature equivalence using the following formula:

$t_A \exp(\frac{-Q}{R.T_A}) = t_B \exp(\frac{-Q}{R.T_B})$, where Q is the activation energy and t_i and T_i are the time and temperature of point i, respectively.

The equivalent time–temperature curves in Fig. 3b confirm the same mechanism at 350 °C and 450 °C, with an activation energy of Q=206 kJ/mol. This activation energy is similar to that proposed by Maetz et al. [4] (Q=185 kJ/mol), which is attributed to the decomposition of ferrite.

3.3. Effect of cold rolling on TEP evolution during aging

To quantify the effect of deformation on the aging behavior of the ferrite, aging at 450 °C was performed after cold rolling to 30% and 50% deformation. This temperature was selected as it results in the highest kinetics of phase separation, with the same phase transformation mechanism as that observed at lower temperatures. The evolution of TEP with aging time at 450 °C for the undeformed and deformed samples is shown in Fig. 4. Increased deformation resulted in a greater TEP increase with aging time. For instance, the same TEP value attained after 1000 h of aging in the undeformed sample was reached after 100 h in the sample cold rolled to 30% deformation and after 3 h for the sample cold rolled to 50% deformation.

This increase in TEP after cold rolling may have three different sources. First, the decomposition kinetics of the ferrite could be enhanced by the higher stress state, as evidenced by [16,17], leading to higher TEP values for a deformed sample than an undeformed one. Sec-

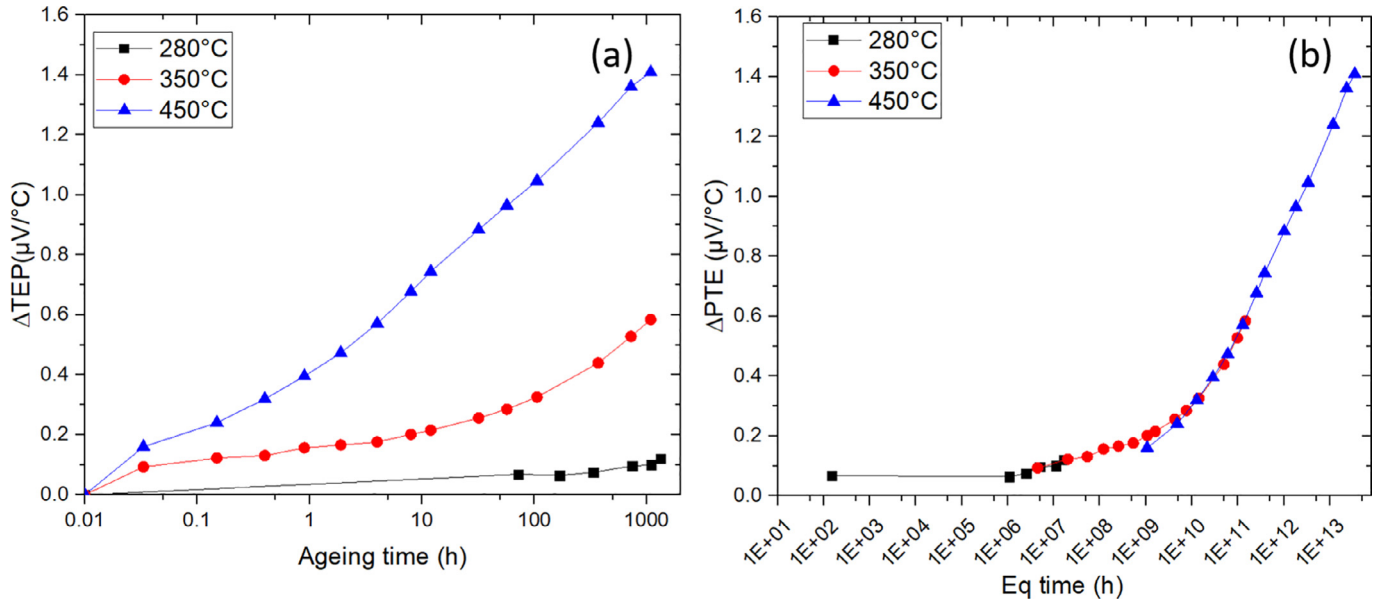

Fig. 3. Effect of aging on the undeformed sample: (a) TEP measurements at 280 °C, 350 °C, and 450 °C after aging for 1 min to 1086 h for the undeformed sample, (b) time–temperature equivalence at room temperature using activation energies of Q= 206 kj.mol^{-1} for aging at 350 °C and 450 °C.

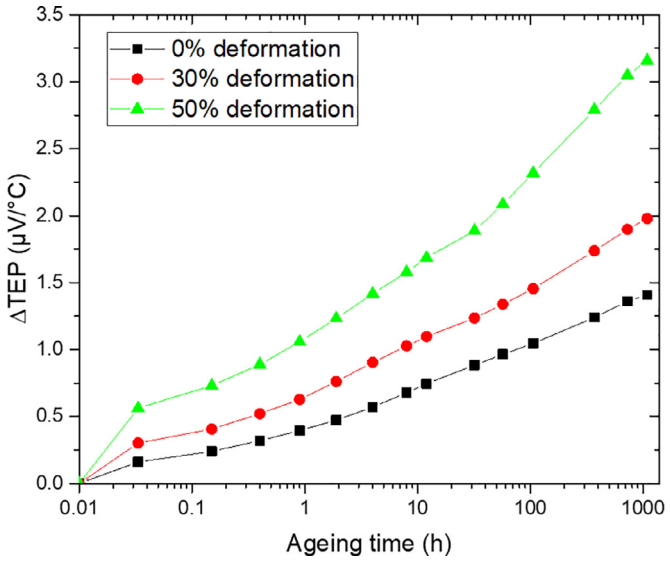

Fig. 4. TEP evolution during 450 °C aging for undeformed and deformed samples.

ond, as martensite is formed during cold rolling by destabilization of austenite, it will inherit the Cr content of the parent phase, which is considered to be very similar to that of ferrite a priori (even if not fully confirmed by APT analyses, as shown in Table 3). Similar to ferrite, martensite is therefore likely to decompose during thermal aging. Thus, for samples cold rolled to 30% and 50% thickness reduction, the proportion of phases prone to decompose (body-centered cubic (BCC) ferrite or martensite) increases, which automatically leads to a higher increase in TEP. Finally, martensite, which should inherit the parent austenite composition, contains higher interstitial (N and C) contents than ferrite. Because of the low solubility of interstitials in BCC structures, this may lead to additional precipitation phenomena, such as nitride or carbide precipitation [35], in the investigated temperature range, affecting the TEP values. To better describe the effect of deformation on phase separation kinetics, the aging products were characterized by APT for the undeformed and cold-rolled conditions.

3.4. APT investigation of microstructural evolution

To correlate the TEP with the micro/nanostructural evolution, selected samples were characterized using APT after 1086 h of aging at 350 °C and 450 °C for the undeformed sample and after 1086 h of aging at 450 °C for the 50% deformed sample.

3.4.1. Phase composition

As aged ferrite (austenite) can be easily identified in undeformed samples by the presence (absence) of Cr content fluctuations, it is straightforward to identify both phases and correlate the phase nature and mass spectra specificities. The situation differs after cold rolling to 50% thickness reduction and 1086 h of aging at 450 °C, with the additional presence of martensite. Again, austenite was identified by the absence of any Cr content fluctuations, and ferrite was identified by the presence of α–α' decomposition. Then, identification of martensite was straightforward; as will be discussed later, martensite is associated with the intense precipitation of chromium nitrides, with the presence of some other additional phases that are not observed in undeformed ferrite or austenite. Typical mass spectra for both ferrite and austenite are shown in Fig. 5, with a focus on the regions exhibiting clear differences.

The two main differences between the mass spectra of ferrite and austenite are the absence/presence of C- and N-related peaks. This finding is in good agreement with the ability of austenite to incorporate larger amounts of interstitials than ferrite. Although C peaks are clearly observed (at 6 and 12 Da for C monoatomic ions and 18 Da for C_3 molecular ions), the situation is less trivial for nitrogen. The first obvious evidence of the presence of nitrogen is the existence of MoN^{2+} molecular ions in the range of 53–57 Da. This tendency of N to form molecular ions with metal ions has been widely reported in the literature [36–38]. In this stainless steel, Mo, V, Cr, and Fe form such molecular ions. In the remainder of this paper, nitrogen detected as molecular ions will be reported as 'combined N'. Nitrogen is also detected as monoatomic ions at 14 Da; however, its quantification is difficult because this 14-Da peak overlaps with that of the main Si isotope, $^{28}Si^{2+}$. A thorough examination of the 14-Da peaks in Fig. 5 reveals their different shapes in ferrite and austenite, with a larger tail observed for the latter. This tail can be attributed to the presence of nitrogen, which is virtually absent from ferrite. Because of the insufficient mass resolution of the instrument used, it was not possible to discriminate between the contributions

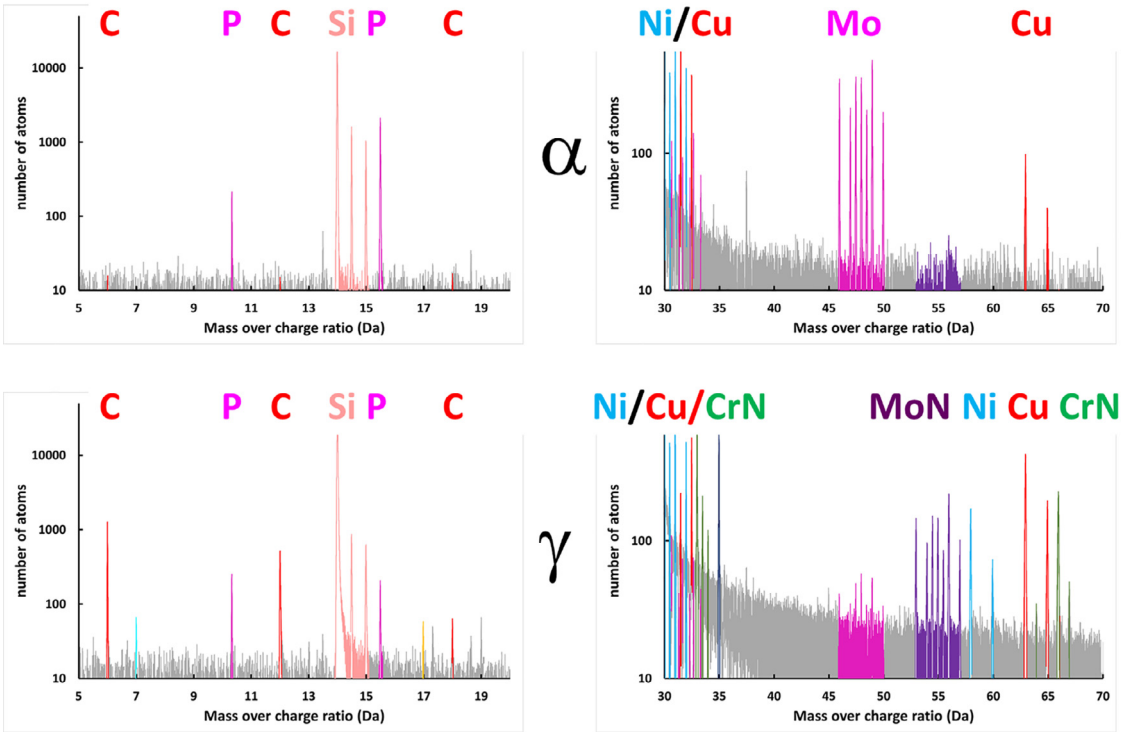

Fig. 5. Mass spectra of ferrite and austenite, with a focus on the regions where the differences are the most obvious. Both spectra contain 65×10^6 ions and were plotted using the IVAS background correction.

and thus obtain an accurate quantification of both species. However, a semi-quantitative approach based on the use of the natural abundance of the three Si isotopes leads to the conclusion that approximately 65% of the 14-Da peak in austenite can be attributed to N. In the rest of the paper, the contribution of the peaks at 14, 14.5, and 15 Da will be reported as 'Si+N'. For ferrite, because of the absence of N, this contribution is purely Si, whereas for austenite, knowing the natural abundance of ^{28}Si (92.22%), the respective contributions of Si and N are estimated to be approximately 40% and 60%, respectively. In aged martensite, Si and N were also shown to be present in the 14-Da peak in the same proportions as in austenite.

The compositions of the different phases, as derived from individual peak identification, are reported in Table 3. It should be noted that analyses conducted in the cold-rolled condition led to smaller investigated volumes (typically 5×10^6 ions per run) because of the brittleness of the sample during APT experiments. The volumes for this state may therefore suffer from lack of representativity compared with those in the undeformed condition (typically 100×10^6 ions).

The compositions measured for ferrite and austenite in the undeformed condition are in good agreement with the nominal ones for the 2202 alloy specification (see Table 1). Unlike Cr, which does not partition between ferrite and austenite, all the other elements tend to partition to austenite (Ni, Mn, C, and N and to a lower extent V and Cu) or ferrite (Mo and P). The low values of the standard deviations indicate that both phases are quite homogeneous, at least in the undeformed condition, where no differences were observed between the samples aged at 350°C and 450 °C. In the deformed condition, the standard deviations for the ferrite and austenite compositions were slightly higher, possibly indicating that slightly larger compositional heterogeneities were generated by the cold-rolling process. The situation differed for martensite, where the standard deviations were much larger than those in the other phases. This is clearly due to the combination of large CrN precipitates (at least several tens of nanometers) and the smaller volumes investigated by APT (typically $40 \times 40 \times 100$ nm^3). Indeed, the measured compositions will be affected by one more or one less large CrN interception by the analyzed volumes. This is also the most likely explanation for the relatively low Cr composition of martensite reported in Table 3.

Regarding Si, and due to the Si/N overlap at 14 Da, the compositions displayed in Table 3 may be confusing. Indeed, it must be kept in mind that for austenite and martensite only 40% of the 'Si+N' value is Si. Table 4 displays the total estimated Si and N contents of austenite and martensite when the contribution of the 14-Da peak is split into Si and N according to the estimated 60% contribution of N to this peak. With this correction, the Si content in austenite is reduced to 0.72 at% compared to the 1.08 at% in ferrite, indicating that Si is clearly segregated in the latter, as expected for an alpha-forming element. The total nitrogen content is increased to approximately 1.6 at% in undeformed austenite and up to 2 at% in martensite.

3.4.2. *Nanostructure of austenite*

The evolution of the austenite nanostructure with aging was investigated by APT in both the undeformed and deformed samples. For all the conditions investigated, 3D reconstructions did not reveal any redistribution of the elements in austenite. This finding was confirmed by the statistical analysis of the spatial distribution of the alloying elements. The reconstructed volumes were split into small sub-volumes of approximately 1 nm^3, and the distribution of the compositions of these volumes was compared with the distribution simulating a random distribution, i.e., the binomial distribution. To illustrate this randomness, both the experimental and binomial distributions are plotted for all the investigated conditions in Fig. 6. The variation (V) was calculated for all these conditions and was smaller than 0.03, which is usually interpreted as evidence of a random solid solution, with deviations from 0 being caused by statistical fluctuations.

3.4.3. *Nanostructure of ferrite*

In contrast to the observations for austenite, the distributions of Cr atoms in the ferritic samples were no longer homogeneous for all investigated conditions, as shown in the 3D reconstructions. There is a clear redistribution of chromium atoms at the nanometric scale into Cr-rich

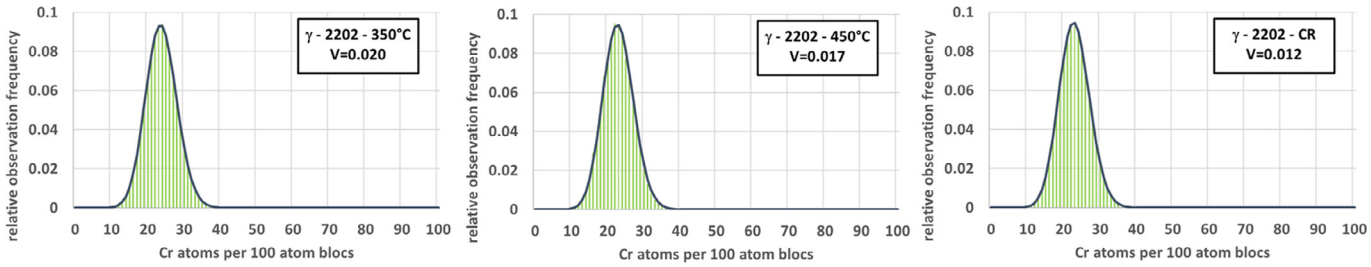

Fig. 6. Experimental and binomial composition frequency distribution and related variation values for the three investigated conditions of austenite, aged for 1086 h at the indicated temperature. CR corresponds to cold rolled and aged at 450 °C.

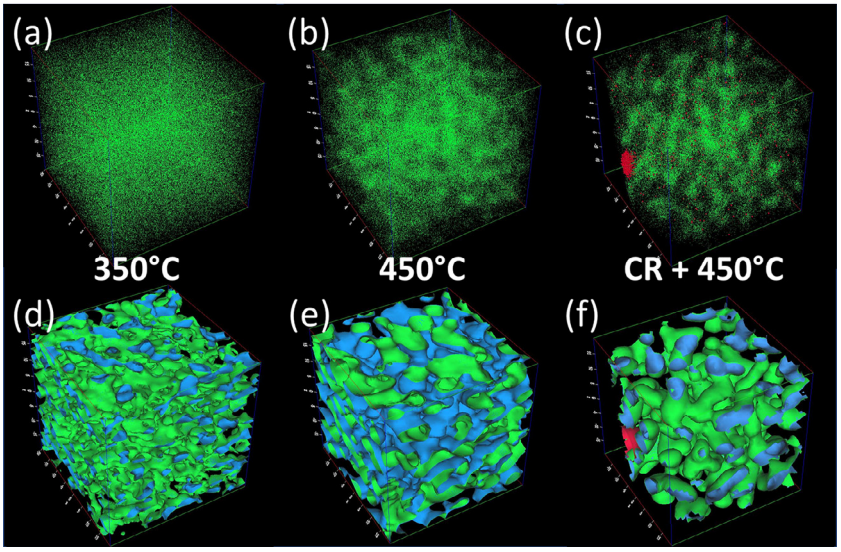

Fig. 7. (a–c) Spatial distribution of Cr atoms and (d–f) corresponding isosurfaces after aging for 1086 h at (a,d) 350 °C and (b,e) 450 °C for the undeformed ferrite and (c,f) at 450 °C after cold rolling. Each individual green dot represents a Cr atom and each red dot represents a Cu atom. The isosurfaces are plotted with a 25 at% Cr threshold; the blue (green) isosurface correspond to the inside (outside) of the Cr-rich domains, with a 2 at% Cu threshold (red). The represented volumes are $40 \times 40 \times 40$ nm^3.

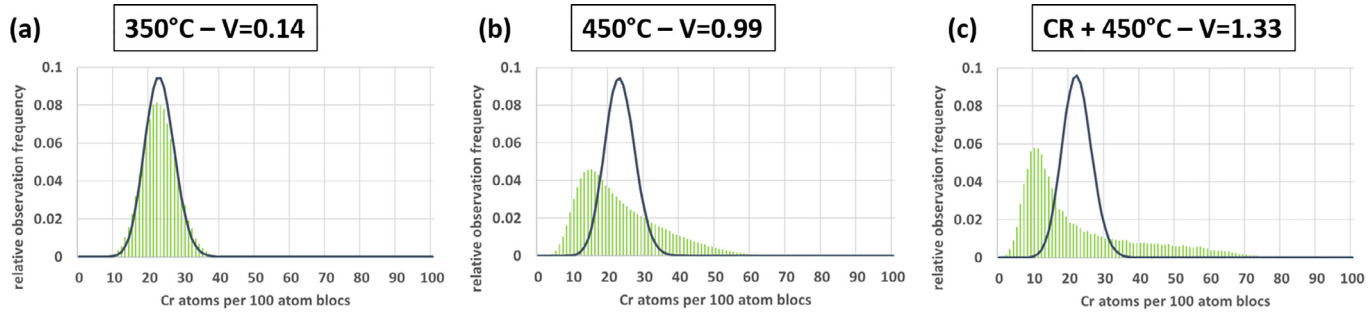

Fig. 8. Experimental and binomial composition frequency distributions and related variation values after aging for 1086 h at (a) 350 °C and (b) 450 °C for the undeformed ferrite and (c) at 450 °C after cold rolling.

α' and Fe-rich α domains, as shown in Fig. 7. Fig. 7(a) and (b) shows the 3D distribution of Cr atoms in selected volumes of $40 \times 40 \times 40$ nm^3 in the undeformed samples. The redistribution of Cr atoms was visually less obvious after aging at 350 °C than at 450 °C; therefore, frequency distribution analyses were conducted to confirm the phase separation.

The results are presented in Fig.8 (a) and (b). For both temperatures, the corresponding experimental composition frequency distributions deviate significantly from the random distribution, represented by the binomial distribution. The measured V values (V=0.13±0.0.1 at 350 °C and V=0.98±0.02 at 450 °C) show that phase separation into Cr-rich α' and Fe-rich α domains occurred at both temperatures.

After aging, the α' and α domains developed an interconnected structure. This structure is revealed by the Cr content isosurface, i.e., the surfaces where the composition is equal to a selected threshold value. When the threshold is set equal to the average content plus one counting statistics standard deviation, the isosurface isolates Cr-rich α' domains. Such isosurfaces are represented in Fig. 7 (d) and (e) for the undeformed aged samples and illustrate the complex morphology of the Cr-rich α' and Fe-rich α domains. Image analysis clearly indicates that for the sample aged at 450 °C, the 25 at% Cr isosurface was continuous over the entire microstructure. In other words, no isolated Cr-rich particles were observed and the structure was fully percolated.

Another way to illustrate phase separation in the ferritic matrix is to plot concentration profiles. Such concentration profiles, plotted with a lateral resolution of 2 nm and a depth resolution of 0.5 nm, are displayed in Fig. 9 (a) and (b) for the corresponding samples. After aging for 1086 h at 350 °C, the composition profile reveals that the maximum Cr content was approximately 45±5 at%, whereas it reached 60±5at% after aging at 450 °C. The characteristic fluctuation wavelengths were measured to be 3±0.5 and 7±0.5 nm, respectively.

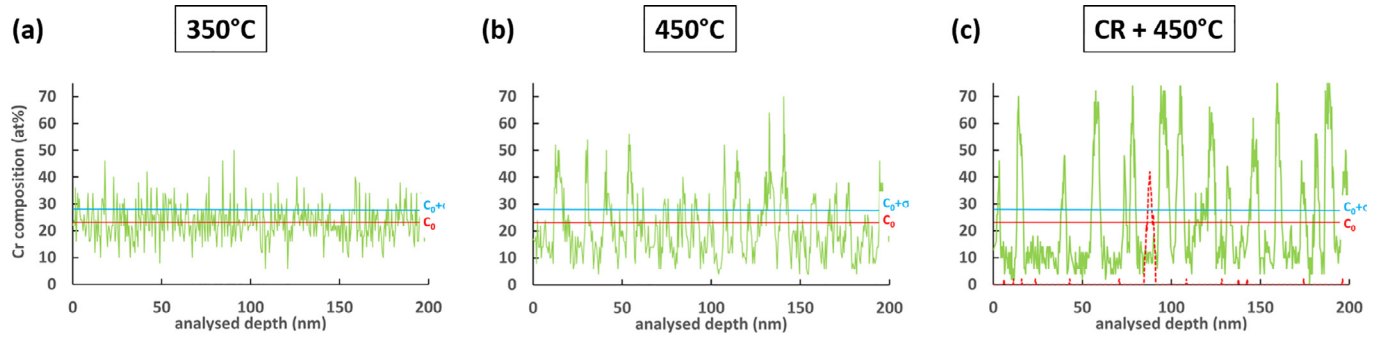

Fig. 9. Cr content profiles extracted from APT 3D reconstructions after aging for 1086 h at (a) 350 °C and (b) 450 °C for the undeformed ferrite and (c) at 450 °C after cold rolling. The red dotted curve in (c) represents the composition of the Cu-rich cluster.

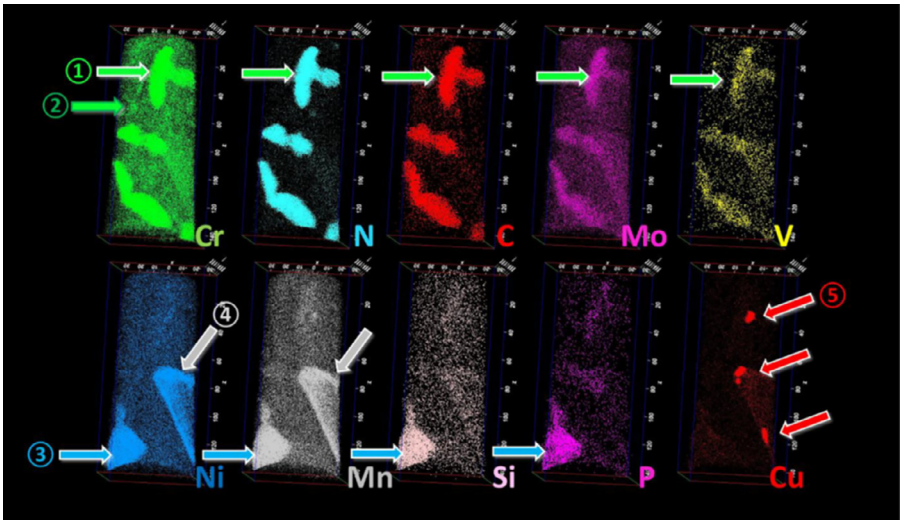

Fig. 10. Elemental distribution in martensite after cold rolling followed by aging for 1086 h at 450 °C. Several types of precipitates were observed: Cr_2N (1, green arrow), nanometric Cr precipitates (2, green arrow), a Ni,Si,Mn,P-enriched phase identified as the G phase (3, blue arrow), Ni- and Mn-rich segregation at the martensite/ferrite interface, which will not be detailed here (4, grey arrow), and a nanocluster enriched in Cu (5, red arrow). Note that the N represented here is only 'combined N'.

To characterize the effect of plastic deformation on the α–α' phase separation process, the material was also investigated for the same aging treatment of 1086 h at 450 °C after cold rolling. The redistribution of Cr atoms and the interconnected structure are clearly observed in Fig. 7 (c) and (f). Once again, the isosurface was continuous throughout the investigated volume. Whereas the V parameter was 0.98 ± 0.02 for the undeformed sample, it was 1.37 ± 0.05 for the previously cold-rolled sample (see Fig. 8 (c)).

In addition to α–α' phase separation, an additional phase-separation process occurs in previously cold-rolled ferrite. As shown in Figs. 7 (c,f) and 9 (c), nanometer-sized Cu clusters were observed after aging. They were observed in most analyses, with a mean diameter of approximately 5 nm and estimated number density of $2 \times 10^{22}/m^3$.

3.4.4. *Nanostructure of (aged) martensite*

Phase separation was also observed in the martensite. First, inheriting the initial Cr content of austenite, which was shown to be very similar to that of ferrite in Table 3, it is expected that Fe–Cr solid solution in martensite will also undergo α–α' phase separation. This phenomenon has been widely reported in the literature [40–43]. Indeed, as shown in Fig. 10, extended Cr content fluctuations were observed in the aged martensite. However, most of the other alloying elements were severely affected by atomic redistribution, which was not the case in ferrite and was used to discriminate between aged ferrite and aged martensite. The first obvious type of precipitates, shown on the first line in the figure and marked as ①, is rather large (tens of nanometers) particles, containing mostly Cr, N, and C and to a lower extent Mo and V. These metallic elements are all known to be nitride formers, and the presence of carbon indicates that they are chromium carbonitrides.

To estimate the compositions of these chromium carbonitride precipitates, they were investigated using the proxigram method [44]. Proxigrams are composition profiles plotted as a function of the distance from any selected surface. The regions with positive (negative) abscissae correspond to the inner (outer) regions delimitated by the isosurface, i.e., regions where the Cr content is higher (lower) than the selected threshold. In this case, we used the 60 at% (Cr+N+C) isosurface, which captured the large chromium carbonitrides, as shown in Fig. 11.

The proxigrams show the evolution of the atomic composition with respect to the distance to the 50 at% Cr isosurface. They clearly reveal a Cr/(N+C) ratio close to 2 in the particles, indicating the $Cr_2(NC)$ nature of the nitrides. The proxigrams also confirm the Mo and V enrichment in the nitrides. In addition, up to 8 at% Fe was also measured in the nitrides, in good agreement with thermodynamic calculations and experimental measurements [45].

In addition to these large $Cr_2(NC)$ particles, many other nanostructural features can be observed, identified as ②, ③, ④, and ⑤ in Fig. 10. The second family, marked as ②, is chromium segregation in the ferritic matrix between the large $Cr_2(NC)$ precipitates. To isolate these precipitates, a reconstruction was generated from which all atoms included in the large carbonitrides were removed. The mean Cr content remaining in the matrix (after removing the large $Cr_2(NC)$ precipitates) was approximately 15 at%. An isosurface with a threshold of 25 at% Cr was then plotted in the remaining volume, as shown in Fig. 12.

The selected threshold is similar to that used in ferrite to demonstrate the interconnected nature of the α–α' phase separation. In aged martensite, the image analysis clearly indicates that these α' domains appear as isolated particles. In addition to these Cr_2N and α' precipitates, many other secondary phases were observed in the aged martensitic, as

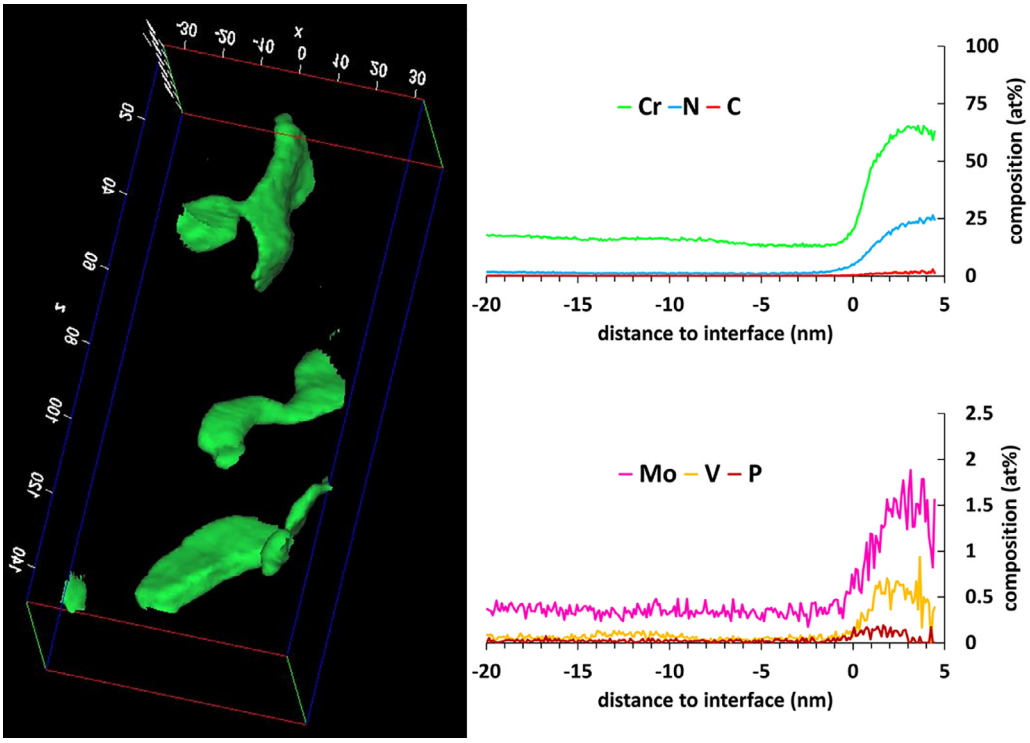

Fig. 11. 50 at% Cr isosurfaces in aged martensite and related proxigram for various elements included in the $Cr_2(NC)$ carbonitrides (à choisir entre les deux versions). The represented volume is 60 × 60 × 140 nm^3. The proxigram was constructed for the large bottom $Cr_2(CN)$ particle.

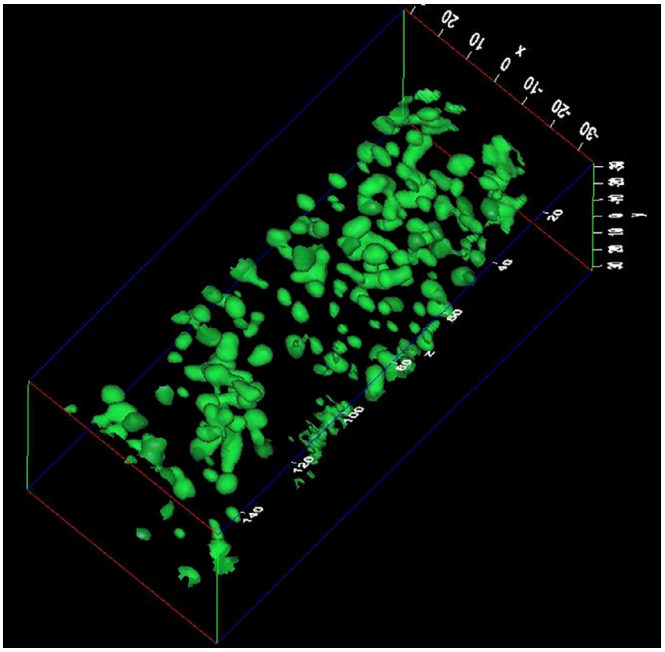

Fig. 12. 25 at% Cr isosurfaces in a volume from which large $Cr_2(NC)$ particles were removed. The represented volume is 60 × 60 × 140 nm^3.

shown in Fig. 10. A large precipitate with high Ni, Si, and Mn contents, marked as ③ and highlighted by a blue arrow, is visible at the bottom left of Fig. 10. A proxigram of this particle, with an isosurface threshold of (Ni+Si+Mn)=50 at%, is presented in Fig. 13.

The composition of this large particle, as listed in Table 4, is very close to the $Ni_{16}Si_7Mn_6$ stoichiometry (54–25–21 in at%), which leads to its identification as a G-phase particle [46]. It clearly appears faceted; however, its size could not be measured as it was cropped by the analyzed volume. Such precipitates have also been observed in 17–4 PH martensitic stainless steels after 5000 of aging at 400 °C [47], with a very similar composition, and in CF8M DSS, where Mo can substitute to [48–50]. Previous TEM and APT results in a 17–4 PH stainless steel suggested that this phase heterogeneously nucleated at pre-existing Cu-precipitate interfaces [47]. In the present case, no Cu-rich precipitates were observed close to the G-phase particle, potentially indicating the same precipitation mechanism. However, as only a part of the G-phase precipitate was present in the analyzed volume, it was not possible to confirm the occurrence of this mechanism. This G-phase particle was the only one intercepted along an analyzed depth of approximately 500 nm. Even if it is impossible to estimate the number density and mean size of these particles without complementary TEM analyses, they most likely have very little effect on the mechanical behavior of the material, and no further investigation was conducted to better characterize this population.

It can also be noted that the proxigram indicates an average Cr content up to 20-nm away in the matrix identical to the initial austenite composition, i.e., 23 at%. This apparent contradiction with the matrix Cr content reported in this section can be explained by the nature of the proxigram. Indeed, as it is plotted as the distance from the G-phase particle interface, it does not differentiate $Cr_2(NC)$ from the matrix and thus provides an averaged Cr content between them, leading to a Cr content close to that of the initial austenite.

Cu nanoprecipitates, marked as ⑤ and highlighted by red arrows in Fig. 10, were also observed in the aged martensite. Their diameter ranged from 5 to 9 nm, their Cu content ranged from 50 at% to 70 at%, and their density was estimated to be 2.2 $10^{22}/m^3$, very similar to in the observations in ferrite for the same treatment. Such precipitates are often observed in aged martensite [16,47,51,52] but for much higher Cu content than in the investigated material.

The precipitation of these Cu clusters is clearly a consequence of the cold rolling, as they were not observed in the undeformed ferrite. If these clusters had been present in the undeformed ferrite with a simi-

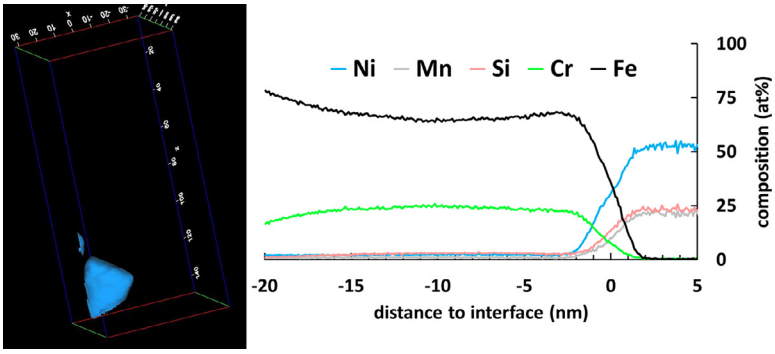

Fig. 13. isoconcentration (Ni+Si+Mn)=50 at% and corresponding proxigram illustrating the presence of a large cropped G-phase particle.

lar number density, they would have inevitably been observed. Indeed, as approximately 2×10^6 nm^3 was analyzed in the undeformed ferrite aged for 1086 h at 450 °C and considering their estimated number density in martensite, approximately 40 Cu particles should have been intercepted, whereas not a single particle was intercepted. It can be assumed that plastic deformation generates a significant linear density of dislocations, which likely favors heterogeneous nucleation of these Cu particles (known to be more energetically favorable than homogeneous nucleation in the absence of dislocations). In addition, cold rolling plays a major role in the precipitation of Cu particles. As no Cu precipitates were detected in the ferrite, it can be concluded that the solubility of Cu in this phase at 450 °C is higher than the measured 0.09 at%. This lower value is slightly higher but not so different from the value of 0.08 at% reported by Miller et al. [53] The Cu enrichment measured in martensite (0.11 at%, as indicated in Table 3) could potentially explain the Cu precipitation but not the depletion observed in ferrite (0.05 at%, as indicated in Table 3). For the latter, the Cu content was clearly lower than the solubility limit; however, precipitation occurred. The thermodynamic reasons for Cu precipitation are not understood in this context but are clearly related to cold rolling and most likely to the presence of an increased density of dislocations.

4. Discussion

4.1. Composition measurements

As shown in Tables 3 and 4, the distributions of C and N were severely affected by cold rolling and subsequent aging and showed a strong tendency to segregate in aged martensite. Indeed, the austenite contained very little C compared to that in the undeformed condition (181 atppm after deformation and 1134 atppm without deformation). Carbon was mostly concentrated in the martensite (1114 atppm) and, more surprisingly, in ferrite to a lesser extent (126 atppm in the cold-rolled condition vs. 28 atppm in the undeformed one). The higher C content in the deformed ferrite can be explained by the presence of numerous lattice defects resulting from plastic deformation, which acted as potential sites for carbon trapping. In addition, the standard deviation for the C content of ferrite was very high (compared with the C content), indicating that some regions were C depleted while others contained more than 200 atppm C. This heterogeneity can be related to the heterogeneity in plastic deformation leading to heterogeneities in carbon segregation between the highly deformed regions (where defects accumulate) and the less deformed ones. A heterogeneously deformed state can result either in local plastic heterogeneity within grains (because of deformation localization) or to a deformation difference from one grain to another (because of the orientation dependence of the deformation). The different grains of the 50% deformed sample are shown in Fig. 14a, and the misorientation distribution is plotted in Fig. 14b. The deformation was quite localized, and some deformation bands appeared (indicated by the white dotted lines). This phenomenon is quite common for ferrite of cold-rolled DSS, where localized strain and dislocation slip bands are developed. However, there is no clear effect of the grain orientation on the deformation state. Therefore, the heterogeneity of the phase separation kinetics is more likely related to the local heterogeneity of deformation.

Table 2
Phase fractions estimated from EBSD for the three different rolling parameters.

	Ferrite	Austenite	Martensite
Rolling 0%	57±5	43±5	0
Rolling 30% thickness reduction	57±5	36±5	6±5
Rolling 50% thickness reduction	57±5	13±5	30±5

The N content in ferrite remained very low (44 atppm) and fairly constant (small standard deviation). The N content in cold-rolled austenite was slightly reduced compared with that in the undeformed one (see Table 4) but clearly increased in martensite, owing to the presence of large chromium nitrides. The martensitic matrix (as defined by excluding large chromium nitrides) exhibited a very low N content of approximately 600 atppm, exclusively observed as 'combined' MoN^{2+} molecular ions. As only aged cold-rolled samples were investigated, it was not possible to determine whether the redistribution of interstitials resulted solely from the cold rolling or subsequent aging or from a combination of cold rolling introducing a high density of defects and aging at 450°C. This combined mechanism can clearly be evoked for interstitial elements that diffuse rapidly at 450°C. Complementary investigations are planned to investigate this specific point of carbon and nitrogen redistribution.

Similar to the observations for the undeformed samples, P and Mo segregated to ferrite, whereas Cu, Mn, and Ni segregated to austenite and martensite. The V content remained rather similar in all the phases. Ni, Mn (Table 3), and Si (Table 4) were also less present in martensite than their original contents in austenite would suggest. This is most likely due to their strong heterogeneous distribution, associated in particular with large G-phase particles. In addition, if one calculates the overall composition of the alloy in the undeformed and cold-rolled conditions (assuming the phase compositions in Tables 3 and 4 and the phase fractions derived from EBSD measurements in Table 2), all the substitutional elements were observed to be depleted in the cold-rolled condition. As all these elements are involved in the precipitation of coarse precipitates in martensite (chromium nitrides, G-phase particles, Cu precipitates, unidentified Ni–Mn phase), which have sizes on the order of the analyzed volumes, it is clearly suspected that our APT analyses do not capture their actual volume fractions. Additional analyses of martensite are necessary to clarify this point.

4.2. Spinodal decomposition in ferrite and effect of cold rolling

As shown in Fig. 7 d and e, the morphologies of the α and α' domains were fully interconnected and percolated. The nature of the developed microstructure strongly suggests that phase separation proceeds through a spinodal decomposition mechanism at this temperature [54].

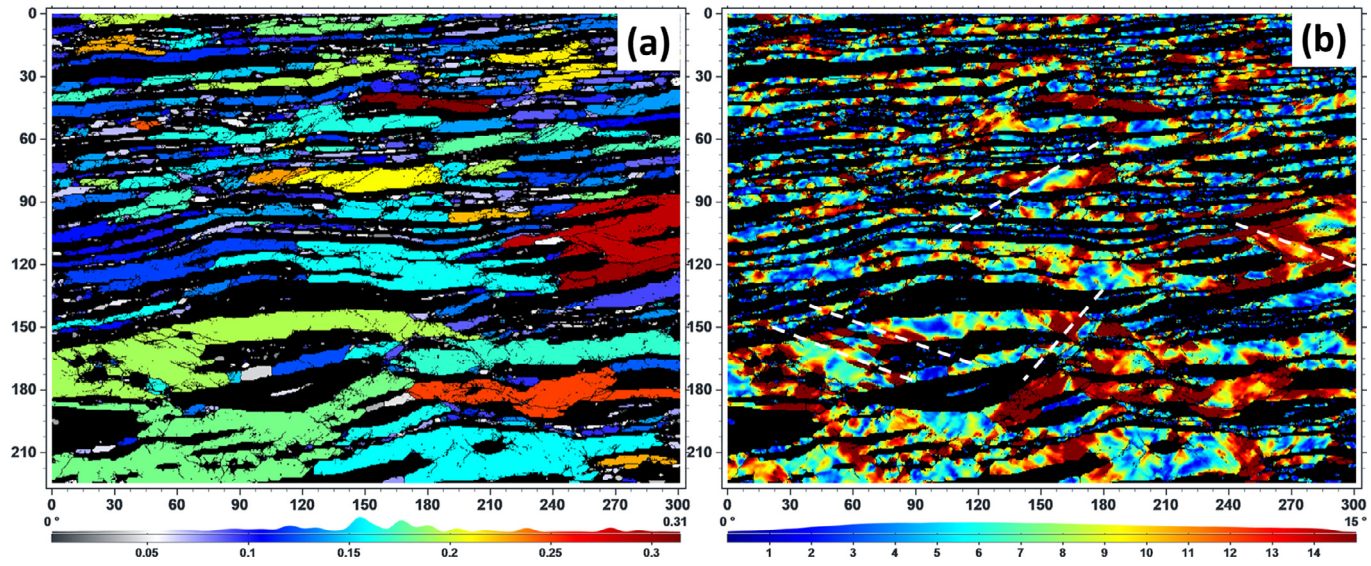

Fig. 14. (a) Grain detection in the ferritic phase after 50% thickness reduction; the grains are colorized as a function of their size, with the smallest colored black and the largest colored red. (b) Corresponding misorientation map, showing a large heterogeneity in the deformation of ferrite.

Table 3
Average APT-measured composition of ferrite and austenite after aging for 1086 h at 350 °C and 450 °C for the undeformed sample and after aging for 1086 h at 450 °C for the deformed sample. The standard deviations were calculated over the composition of individual analyses (at least five analyses per phase, except for martensite (three analyses)), and do not consider counting statistics, [39] which are several orders of magnitude lower than the σ given in the table.

CR level	Phase	Cr at%	Ni at%	Si+N at%	Mo at%	Mn at%	V ppm	Cu ppm	C ppm	Combined N ppm	P Ppm	B ppm
0%												
	ferrite	**23.2**	**2.17**	**1.08**	**0.25**	**1.05**	**700**	**893**	**28**	**170**	**849**	**20**
	σ	*0.2*	*0.03*	*0.03*	*0.01*	*0.02*	*13*	*30*	*26*	*166*	*114*	*20*
	austenite	**23.6**	**3.34**	**1.80**	**0.19**	**1.35**	**754**	**1106**	**1134**	**0.50 at%**	**168**	**64**
	σ	*0.5*	*0.19*	*0.15*	*0.01*	*0.03*	*28*	*84*	*339*	*0.10 at%*	*15*	*6*
	ferrite	**23.0**	**2.00**	**1.09**	**0.24**	**0.99**	**543**	**502**	**126**	**44**	**758**	**28**
	σ	*0.6*	*0.21*	*0.03*	*0.02*	*0.07*	*101*	*230*	*135*	*58*	*246*	*24*
50%	**austenite**	**22.9**	**3.51**	**1.67**	**0.17**	**1.41**	**736**	**995**	**181**	**0.39 at%**	**198**	**108**
	σ	*0.2*	*0.23*	*0.11*	*0.01*	*0.09*	*31*	*85*	*86*	*0.12 at%*	*52*	*39*
	martensite	**19.9**	**2.52**	**1.42**	**0.14**	**1.00**	**519**	**1113**	**1114**	**1.17 at%**	**203**	**68**
	σ	*1.5*	*1.1*	*0.44*	*0.03*	*0.32*	*196*	*842*	*361*	*0.53 at%*	*127*	*29*

Table 4
Estimated Si and N contents of austenite and martensite, considering the 14-Da overlap.

Phase	Undeformed austenite		Deformed austenite		Martensite	
Element	Si	N	Si	N	Si	N
Measured (at%)	**1.80**	**0.50**	**1.67**	**0.39**	**1.42**	**1.17**
Corrected (at%)	**0.72**	**1.58**	**0.67**	**1.39**	**0.57**	**2.02**

This speculation was confirmed by the Cr content profiles, in particular that for aging at 450 °C in Fig. 9 b. It can be clearly observed that the Cr content of the α' domains does not reach 85 at%, which, according to the phase diagram, is the expected equilibrium composition at this temperature. This finding indicates that phase separation does not proceed through the nucleation and growth of equilibrium composition α' precipitates. In addition, a clear evolution is observed between 350 °C and 450 °C aging, characterized by an increase in the α' domain composition and characteristic distances between them. All these elements support a spinodal mechanism being active at 450 °C (and below), even if only a kinetic study (not conducted here) could prove this speculation. This conclusion is fully consistent with previous investigations of ferritic stainless steels containing approximately 20 at% Cr [54]. From a thermodynamical viewpoint, if SD is active at 450 °C, it must also be active at any lower temperature, including 350 °C.

Table 5
Experimental composition of precipitates in martensite.

at %	Fe	Cr	Si	Ni	Mn	Mo	V	Cu	N	C	P	B
$Cr_2(NC)$	9.1	64.6	–	1.0	0.95	0.78	0.54	0.01	21.3	1.5	0.02	0.02
G phase	0.37	0.38	23.4	52.4	21.6	0.23	0.01	0.16	0.12	0.05	1.15	–
Ni-rich phase	69.0	22.1	1.43	4.55	1.5	0.48	0.05	0.2	0.43	0.04	0.03	

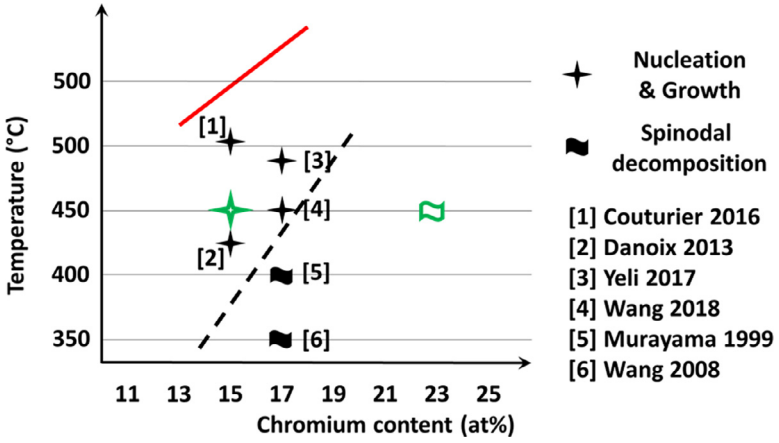

Fig. 15. Fe–Cr phase diagram showing the phase transformation mechanism of the a–a' decomposition process as a function of Cr content and temperature. The dark solid symbols refer to literature data, and the empty green symbols represent the data for the current study. The black dashed line schematically represents the spinodal line, and the solid red line represents the limit of the miscibility gap as proposed by Bonny for ferritic Fe–Cr alloys [57]. Note that the Ni content was not considered.

Regarding the cold-rolled samples, the interconnected nature of the α–α' microstructure indicates that SD is most likely active, with the absence of isolated α' precipitates ruling out a possible NG process. From a kinetic viewpoint, both the frequency distribution analysis (shown in Fig. 8 c) and related composition profile (shown in Fig. 9 c) confirm that the phase separation is more advanced for the cold-rolled specimens after the same aging treatment of 1086 h at 450 °C. The respective mean V values were 1.37±0.05 vs. 0.97±0.03, the maximum Cr content was approximately 70±5 at% vs. 60±5 at%, and the characteristic composition fluctuation wavelengths were 12±0.5 nm vs. 7±0.5 nm. These results unambiguously confirm that the previously cold-rolled samples underwent a faster phase separation than the undeformed samples, providing direct evidence that plastic deformation enhances SD in the ferritic matrix of this Fe–Cr alloy. The most likely reason for this enhancement is the presence of point defects, in particular vacancies, as revealed by the increase in carbon content in the cold-rolled ferrite. The higher number of vacancies naturally accelerates atomic diffusion and thus the SD kinetics. It should also be noticed that the standard deviation of the variation values V is larger for the cold-rolled samples (0.05 vs. 0.02). This result indicates a certain level of heterogeneity in α–α' phase separation that was not observed in the undeformed samples. As for the heterogeneous distribution of C in ferrite, this can be analyzed in light of the plastic strain deformation heterogeneity observed in the ferritic matrix, even if no direct correlation was observed between the V values and local C content.

4.3. Decomposition of martensite: Cr behavior

After deformation and subsequent aging at 450 °C for 1086 h, decomposition of both the ferritic and martensitic phases occurred. Whereas an interconnected structure, attributed to a spinodal mechanism, was observed in ferrite, individual particles were observed in martensite for the same isoconcentration threshold. This change in morphology is associated with a change in the phase-separation process from SD in ferrite to NG in martensite. This change in the decomposition process is related to the matrix composition difference between the two phases. Indeed, the composition of the martensitic matrix was measured to be 15 at%, whereas it was approximately 23 at% in ferrite. Several investigations of α–α' decomposition in martensite have been conducted, where the phase-separation process was identified as a function of temperature and Cr content. These results were compiled and are presented in a Fe–Cr phase diagram in Fig. 15. These investigations were mostly conducted on 15–5 PH, 17–4 PH, and a model 15–5 martensitic stainless steel (where the first and second numbers refer to the Cr and Ni contents, respectively). NG is clearly the active mechanism for the 15 at% Cr from 500 °C to 425 °C [16,51] and for the 17 at% Cr one at 480°C [55], whereas SD is clearly the active mechanism for the 17 at%Cr at 400 °C and below [47]; the situation was less clear for the 17 at% Cr at 450°C according to [56]. It can be concluded that the location of the spinodal (or bimodal) line, represented by the black dashed line, separating the nucleation and growth domain (top left) and spinodal decomposition domain (bottom right), lies at approximately 450 °C for a Cr content of approximately 17 at%, and at increasing (decreasing) temperature for higher (lower) Cr contents. Note that the position of the spinodal line is plotted for illustrative purposes; its slope is purely hypothetical.

The point representing our martensitic alloy at 450 °C (green star in Fig. 15) clearly lies on the left side of the spinodal line, indicating that it should undergo NG of α' rather than the SD observed for the ferritic phase. Assuming that the phase diagram is similar for ferritic and martensitic alloys, the ferrite phase of the investigated alloy (empty green flag) lies deeply in the spinodal decomposition domain. All these results are in perfect agreement with our experimental data, and it can therefore be concluded that the Cr depletion of the martensitic matrix results in a shift from SD (as observed in ferrite) to NG of α' particles in martensite aged at 450 °C.

4.4. Interpretation of TEP measurements concerning microstructural evolution

For the undeformed samples, only ferrite phase separation was observed during aging in the APT characterization. This finding is in good agreement with TEP measurements that show a similar trend for all samples aged between 280 °C and 450 °C, with one mechanism involved, with an activation energy corresponding to ferrite phase separation [4]. This result highlights the efficiency of TEP measurements for the fast detection of decomposition kinetics in metals. Indeed, the TEP increase was significant even at relatively low temperatures and fast heat treatments (such as $\Delta TEP = 0.1\ \mu V/°C$ after 1 h at 350 °C), where the phase separation process must give rise to very small composition variations that are difficult to detect even with powerful techniques such as APT but that can be detected with much more time-consuming techniques, such as Mössbauer spectrometry [8].

For the deformed samples, APT characterization revealed that not only ferrite phase separation but also complex precipitation and demixing occurred in martensite during aging. A time–temperature equivalence analysis was performed for the deformed samples after aging at 450 °C. For the three samples, the activation energy was set to 206 kJ/mol, which corresponds to the ferrite phase separation, and the temperature of the undeformed sample was set to 450 °C. For the 30% and 50% deformed samples, selecting temperatures of 500 °C and 570 °C, respectively, enabled the three curves to be superimposed. This finding highlights the fact that all three samples were subjected to ferrite phase separation. The fictive temperature increase of the deformed samples confirms the acceleration in kinetics observed by APT. Moreover, one can see that for an equivalent time of 1.10^{25} h, the curve corresponding to the 50% deformed sample starts to diverge from the

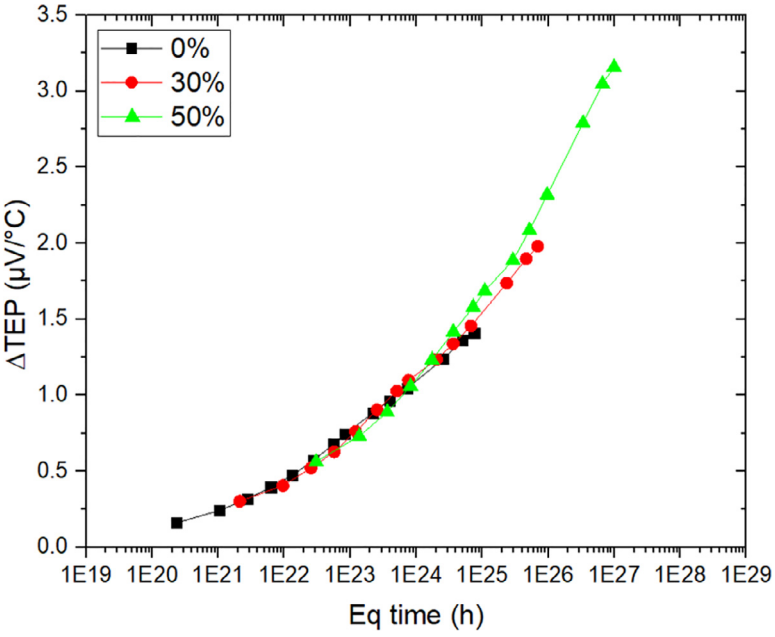

Fig. 16. Pseudo time–temperature equivalence plotted for the deformed samples using an activation energy of 206 kJ/mol. The temperature of the undeformed sample was set to 450 °C, with equivalent temperatures of 500 °C and 570 °C for the 30% and 50% deformed ones, respectively, resulting in the three curves being superimposed.

other two. This result corresponds to approximately 10 h of aging at 450 °C and could be a sign of the start of the other microstructural evolutions observed from APT: precipitation and martensite decomposition (Fig. 16).

5. Conclusion

In this study, the effect of cold rolling on the aging response at intermediate temperatures (lower than 450 °C) of a lean 2202 duplex stainless steel was investigated by comparing the thermal response of undeformed and cold-rolled samples.

In the undeformed samples, no elemental redistribution was observed in austenite was by thermal aging up to 450 °C, whereas ferrite decomposed into α-Fe rich and α'-Cr rich domains via spinodal decomposition. The activation energy of this process was measured to be 206 kJ/ml.

Cold rolling led to the transformation of austenite into martensite, whereas the fraction of ferrite remained unaffected. Interstitial elements were redistributed between the three phases, with a strong enrichment in carbon and nitrogen of martensite.

Cold-rolling enhances enhances ferrite decomposition, which still followed a α–α' spinodal decomposition mechanism and developed α–α' microstructure in terms of composition fluctuation amplitudes and characteristic wavelength. Second, martensite, which formed during austenite deformation, was also shown to be a site for phase transformations, including α–α' decomposition and precipitation of large $Cr_2(NC)$, G-phase, and Cu-rich particles. α–α' decomposition of the martensitic matrix follows a nucleation and growth process. This change in α–α' decomposition is due to Cr depletion in the matrix, resulting from the intense precipitation of $Cr_2(NC)$, consistent with the most recent Fe–Cr phase diagrams.

This study has demonstrated the complementarity of TEP and APT in investigating aging in DSSs, combining the overall response of the material to TEP with the ability of APT to quantitatively characterize the microstructure of selected samples at the nanometer scale. The combination of these techniques provides a detailed understanding of the aging response to cold rolling in DSSs.

Data availability

The raw/processed data will be made available on request.

Declaration of Competing Interest

The authors declare that they have no known competing financial interests or personal relationships that could have appeared to influence the work reported in this paper.

Acknowledgments

This work was partly performed using the experimental GENESIS platform, supported by the Region Haute-Normandie, Metropole Rouen Normandie, CNRS via LABEX EMC, and French National Research Agency as part of the program "Investissements d'avenir" under reference ANR-11-EQPX-0020.

References

[1] J.-O. Andersson, E. Alfonsson, C. Canderyd, Development and Properties of New Duplex Stainless Steels, (2010) 23.
[2] M. Liljas, P. Johansson, H.-P. Liu, C.-O.A. Olsson, Development of a lean duplex stainless steel, Steel Res. Int. 79 (2008) 466–473.
[3] J.-Y. Maetz, S. Cazottes, C. Verdu, X. Kleber, Precipitation and phase transformations in 2101 lean duplex stainless steel during isothermal aging, Metall. Mater. Trans. A 47 (2016) 239–253.
[4] J.-Y. Maetz, S. Cazottes, C. Verdu, F. Danoix, X. Kléber, Microstructural evolution in 2101 lean duplex stainless steel during low-and intermediate-temperature aging, Microsc. Microanal. 22 (2016) 463–473.
[5] S.S. Brenner, M.K. Miller, W.A. Soffa, Spinodal decomposition of iron-32 at.% chromium at 470°C, Scr. Metall. 16 (1982) 831–836.
[6] J.E. Brown, G.D.W. Smith, Atom probe studies of spinodal processes in duplex stainless steels and single- and dual-phase Fe-Cr-Ni alloys, Surf. Sci. 246 (1991) 285–291.
[7] F. Danoix, P. Auger, Atom probe studies of the Fe–Cr system and stainless steels aged at intermediate temperature: a review, Mater. Charact. 44 (2000) 177–201.
[8] C. Lemoine, A. Fnidiki, J. Teillet, M. Hédin, F. Danoix, Mössbauer study of the ferrite decomposition in unaged duplex stainless steels, Scr. Mater. 39 (1998) 61–66.
[9] M.K. Miller, J.M. Hyde, A. Cerezo, G.D.W. Smith, Comparison of low temperature decomposition in Fe Cr and duplex stainless steels, Appl. Surf. Sci. 87–88 (1995) 323–328.
[10] M.K. Miller, K.F. Russell, Comparison of the rate of decomposition in Fe 45%Cr, Fe 45%Cr 5%Ni and duplex stainless steels, Appl. Surf. Sci. 94–95 (1996) 398–402.
[11] D.A. Porter, K.E. Easterling, Phase Transformations in Metals and Alloys, Chapman & Hall, 1993.
[12] D.A. Garfinkel, J.D. Poplawsky, W. Guo, G.A. Young, J.D. Tucker, Phase separation in lean-grade duplex stainless steel 2101, JOM 67 (2015) 2216–2222.
[13] J.D. Tucker, M.K. Miller, G.A. Young, Assessment of thermal embrittlement in duplex stainless steels 2003 and 2205 for nuclear power applications, Acta Mater. 87 (2015) 15–24.
[14] A. Dahlstrom, Influence of a Mechanical Load on the Ageing of Fe-Cr Alloys, Université de Rouen, 2019.

[15] Y.-S. Li, H. Zhu, L. Zhang, X.-L. Cheng, Phase decomposition and morphology characteristic in thermal aging Fe–Cr alloys under applied strain: a phase-field simulation, J. Nucl. Mater. 429 (2012) 13–18.

[16] F Danoix, et al., Effect of external stress on the Fe–Cr phase separation in 15-5 PH and Fe–15Cr–5Ni alloys, Ultramicroscopy 132 (2013) 193–198.

[17] J. Zhou, J. Odqvist, M. Thuvander, S. Hertzman, P. Hedström, Concurrent phase separation and clustering in the ferrite phase during low temperature stress aging of duplex stainless steel weldments, Acta Mater. 60 (2012) 5818–5827.

[18] J.K. Sahu, U. Krupp, R.N. Ghosh, H.-J. Christ, Effect of 475°C embrittlement on the mechanical properties of duplex stainless steel, Mater. Sci. Eng. A 508 (2009) 1–14.

[19] C. Örnek, M.G. Burke, T. Hashimoto, D.L. Engelberg, 748 K (475 °C) Embrittlement of duplex stainless steel: effect on microstructure and fracture behavior, Metall. Mater. Trans. A 48 (2017) 1653–1665.

[20] M. Hättestrand, P. Larsson, G. Chai, J.-O. Nilsson, J. Odqvist, Study of decomposition of ferrite in a duplex stainless steel cold worked and aged at 450–500°C, Mater. Sci. Eng. A 499 (2009) 489–492.

[21] F. Iacoviello, F. Casari, S. Gialanella, Effect of “475 °C embrittlement” on duplex stainless steels localized corrosion resistance, Corros. Sci. 47 (2005) 909–922.

[22] V. Seetharaman, R. Krishnan, Influence of the martensitic transformation on the deformation behaviour of an AISI 316 stainless steel at low temperatures, J. Mater. Sci. 16 (1981) 523–530.

[23] M. Perez, V. Massardier, X Kleber, Thermoelectric power applied to metallurgy: principle and recent applications, Int. J. Mater. Res. 100 (2009) 1461–1465.

[24] N. Lavaire, V. Massardier, J. Merlin, Quantitative evaluation of the interstitial content (C and/or N) in solid solution in extra-mild steels by thermoelectric power measurements, Scr. Mater. 50 (2004) 131–135.

[25] J.M Pelletier, et al., Precipitation effects on thermopower in Al-Cu alloys, Acta Metall. 32 (1984) 1069–1078.

[26] A. Lamontagne, X. Kleber, V. Massardier, D. Mari, Application of Thermoelectric Power Technique to Study The Static Strain Ageing of Heavily Cold Drawn Steel. (2013).

[27] B. Beausir, J.-J. Fundenberger, Analysis Tools for Electron and X-ray Diffraction, ATEX - Software, Université de Lorraine - Metz, 2017 www.atex-software.eu.

[28] M Labonne, et al., Precipitation kinetics in a Nb-stabilized ferritic stainless steel, Metall. Mater. Trans. A 48 (2017) 3655–3664.

[29] B. Gault, M.P. Moody, J.M. Cairney, S.P. Ringer, Atom Probe Microscopy, 160, Springer, New York, NY, 2012.

[30] L. Vonalvensleben, R. Grune, A. Hutten, M. Oehring, Statistical analysis of atom probe data, J. Phys. 47 (1986) 489–494.

[31] P Bassani, et al., Characterization of a cold-rolled 2101 lean duplex stainless steel, Microsc. Microanal. 19 (2013) 988–995.

[32] S.S.M. Tavares, Pardal, J.M. Silva, M.R. da & Oliveira, C.A.S. de, Martensitic transformation induced by cold deformation of lean duplex stainless steel UNS S32304, Mater. Res. 17 (2013) 381–385.

[33] J.F. Coste et al. *Application of Thermoelectricity to NDE of Thermally Aged Cast Duplex Stainless Steels and Neutron Irradiated Ferritic Steels*. 16, https://inis.iaea.org/collection/NCLCollectionStore/_Public/30/001/30001866.pdf?r=1&r=1 (1997).

[34] J.-P Massoud, et al., Thermal aging of PWR duplex stainless steel components development of a thermoelectrical technique as a non-destructive evaluation method of aging, in: Proceedings of the 7th International Conference on Nuclear Engineering, ICONE-7243, 1999.

[35] P. Jessner, R. Danoix, B. Hannoyer, F. Danoix, Investigations of the nitrided subsurface layers of an Fe–Cr-model alloy, Ultramicroscopy 109 (2009) 530–534.

[36] H.-O. Andrén, U. Rolander, G. Wahlberg, Molybdenum-nitrogen and molybdenum–carbon complex formation in steels, J. Phys. Colloq. 49 (1988) C6-305-C6-310.

[37] S.S. Brenner, S.R. Goodman, FIM-atom probe analysis of thin nitride platelets in Fe-3 at.% Mo, Scr. Metall. 5 (1971) 865–869.

[38] A Deschamps, et al., Low temperature precipitation kinetics of niobium nitride platelets in Fe, Mater. Lett. 65 (2011) 2265–2268.

[39] F. Danoix, G. Grancher, A. Bostel, D. Blavette, Standard deviations of composition measurements in atom probe analyses—Part II: 3D atom probe, Ultramicroscopy 107 (2007) 739–743.

[40] D Delagnes, et al., Cementite-free martensitic steels: A new route to develop high strength/high toughness grades by modifying the conventional precipitation sequence during tempering, Acta Mater. 60 (2012) 5877–5888.

[41] T.J. Kinkus, G.B. Olson, Microanalytical evaluation of a prototype stainless bearing steel, Surf. Sci. 266 (1992) 391–396.

[42] K. Stiller, F. Danoix, M. Hättestrand, Mo precipitation in a 12Cr–9Ni–4Mo–2Cu maraging steel, Mater. Sci. Eng. A 250 (1998) 22–26.

[43] M. Thuvander, M. Andersson, K. Stiller, Precipitation process of martensitic PH stainless steel Nanoflex, Mater. Sci. Technol. 28 (2012) 695–701.

[44] O.C. Hellman, J.A. Vandenbroucke, J. Rüsing, D. Isheim, D.N. Seidman, Analysis of three-dimensional atom-probe data by the proximity histogram, Microsc. Microanal. 6 (2000) 437–444.

[45] H Van Landeghem, et al., Contribution of local analysis techniques for the characterization of iron and alloying elements in nitrides: consequences on the precipitation process in Fe–Si and Fe–Cr nitrided alloys, Materials 11 (2018) 1409.

[46] H.J. Beattie, F.L. VerSnyder, A new complex phase in a high-temperature alloy, Nature 178 (1956) 208–209.

[47] M. Murayama, K. Hono, Y. Katayama, Microstructural evolution in a 17-4 PH stainless steel after aging at 400 °C, Metall. Mater. Trans. A 30 (1999) 345–353.

[48] F. Danoix, P. Auger, S. Chambreland, D. Blavette, A 3D study of G-phase precipitation in spinodally decomposed α-ferrite by tomographic atom-probe analysis, Microsc. Microanal. Microstruct. 5 (1994) 121–132.

[49] T.R. Leax, S.S. Brenner, J.A. Spitznagel, Atom probe examination of thermally ages CF8M cast stainless steel, Metall. Trans. A 23 (1992) 2725–2736.

[50] M.K. Miller, J. Bentley, APFIM and AEM investigation of CF8 and CF8M primary coolant pipe steels, Mater. Sci. Technol. 6 (1990) 285–292.

[51] L. Couturier, F. De Geuser, A. Deschamps, Direct comparison of Fe-Cr unmixing characterization by atom probe tomography and small angle scattering, Mater. Charact. 121 (2016) 61–67.

[52] Habibi Bajguirani, H. R., The effect of ageing upon the microstructure and mechanical properties of type 15-5 PH stainless steel, Mater. Sci. Eng. A 338 (2002) 142–159.

[53] M.K. Miller, K.F. Russell, P. Pareige, M.J. Starink, R.C. Thomson, Low temperature copper solubilities in Fe–Cu–Ni, Mater. Sci. Eng. A 250 (1998) 49–54.

[54] J. Zhou, J. Odqvist, M. Thuvander, P. Hedström, Quantitative evaluation of spinodal decomposition in Fe-Cr by atom probe tomography and radial distribution function analysis, Microsc. Microanal. 19 (2013) 665–675.

[55] G Yeli, et al., Sequential nucleation of phases in a 17-4PH steel: microstructural characterisation and mechanical properties, Acta Mater. 125 (2017) 38–49.

[56] J. Wang, H. Zou, C. Li, S. Qiu, B. Shen, The spinodal decomposition in 17-4PH stainless steel subjected to long-term aging at 350 °C, Mater. Charact. 59 (2008) 587–591.

[57] G. Bonny, D. Terentyev, L. Malerba, On the α–α' miscibility gap of Fe–Cr alloys, Scr. Mater. 59 (2008) 1193–1196.